

Structural and Electrochemical Insights from the Fluorination of Disordered Mn-Based Rock Salt Cathode Materials

Yasaman Shirazi Moghadam, Sirshendu Dinda, Abdel El Kharbachi,* Georgian Melinte, Christian Kübel, and Maximilian Fichtner*



Cite This: *Chem. Mater.* 2022, 34, 2268–2281



Read Online

ACCESS |



Metrics & More

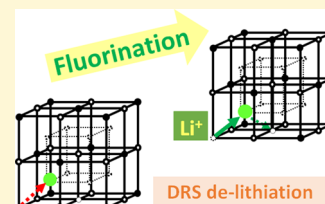


Article Recommendations



Supporting Information

ABSTRACT: Recent studies have shown that disordered rock salt (DRS) oxyfluorides with Li excess are interesting candidates as cathode materials for Li-ion batteries. However, these materials have not been able to achieve the desired technological level yet owing to structure stability issues and the lack of direct evidence of the underlying Li⁺ (de)insertion mechanism. In this work, we demonstrate how fluorine can increase the stability of the DRS structure and improve the lithium diffusion in a percolation network concomitant with accommodated structural Mn oxidation. Therefore, we synthesized four representative Mn-based DRS materials in the Li_{1+x}Mn_{2/3}Ti_{1/3}O₂F_x (0 ≤ x ≤ 1) chemical system to clarify the effect of fluorine on the structural and electrochemical properties. All of the compositions have achieved higher than 210 mAh g⁻¹ initial capacity and good cyclability, mainly for high F/Li ratios. The ex situ Raman spectroscopy analysis shed light on the lithium diffusion pathways inside the structure and on the effect of fluorine on the Li⁺ (de)insertion during cycling. Thanks to the F-enrichment, the amount of Li⁺ trapped as LiO₄ tetrahedral sites can be reduced, allowing more efficient lithium transport. The structure stability is reinforced by its Mn^{II}O₆ octahedral local ordering, resulting in better capacity retention. The study demonstrates the viability of the fluorination strategy toward developing cobalt-free cathode materials with enhanced performance.



INTRODUCTION

In today's multiple-speed battery technology, high capacity and safe Co-free cathode materials for Li-ion batteries (LIBs) are key for the development of next-generation electric vehicles and energy storage systems.^{1,2} As an alternative to the currently commercialized materials (e.g., lithium–cobalt oxide (LCO), nickel–manganese–cobalt (NMC), and nickel–cobalt–aluminum (NCA)), LiMn₂O₄ and LiFePO₄ have emerged as intercalation cathode candidates, which present the advantage of being abundant and environmentally friendly. However, they have comparably low practical capacities of around 148 and 170 mAh g⁻¹, respectively.^{3–5} Therefore, more efforts are necessary to explore new cathode materials and chemistries while targeting sustainable LIB-based storage systems with high energy density. Durability and cycling performance, along with rate capability, are major issues that need to be reconsidered.^{6,7}

Recent studies have shown that lithium-excess disordered rock salt (DRS) materials may pave the way to an increased specific capacity while allowing for sufficiently fast kinetics.^{7,8} In fact, they can demonstrate the formation of appropriate percolation pathways within the rock salt structure to support ionic diffusion and facilitate the (dis)charging processes. The cation disorder, by its high entropy contribution, is able to improve the structural and thermodynamic stability, while the increased lithium content enhances the kinetics.^{2,9} Although several lithium-excess phases such as Li₃V₂O₅, Li₂VO₃, Li₂VO₃, or Li₃NbO₄ have shown high capacities (~300 mAh g⁻¹),^{7,10,11}

disordered cathode materials based on manganese such as Li₂MnO₂F may have several advantages over vanadium, such as low cost, ease of synthesis, great stability, and environmental friendliness.^{12,13} Similar to the Li₂MnTiO₄ reduced spinel,¹⁴ design strategies based on density functional theory (DFT) have suggested combining redox-inactive transition metals (TMs) such as Ti for improving the stability of the structure and lowering the volume change during cycling.¹⁵ The beneficial effect of titanium on the DRS structure based on Mn was investigated, and it was found that Ti-rich compositions could have an adverse effect on the electrochemical stability owing to the presence of two competitive active TMs.^{16,17}

In addition, if O anions get partially substituted by F anions, the structure would be stabilized; hence, the electrochemical properties can be enhanced. This is a widely used strategy, which was introduced by Chen et al.,¹⁸ since fluorination can allow a large oxidation state of the TM, for instance, Mn, by making the Li–O bonds weaker. It can induce more Mn^{III} vacancies, which would reduce the energy barrier of Li⁺ migration in the crystal structure and improve the electronic

Received: November 24, 2021

Revised: February 4, 2022

Published: February 17, 2022



transmission performance.^{19,20} On the other hand, based on previous studies, fluorine substitution can also protect the electrode from HF attack.²¹ This approach resulted in the synthesis of several cathode materials such as $\text{Li}_2\text{VO}_2\text{F}$, $\text{Li}_2\text{CrO}_2\text{F}$, and $\text{Li}_2\text{MoO}_2\text{F}$, all of which showed high capacity.^{18,22,23} Note that fluorine incorporation is expected to influence the Li^+ percolation network due to the large bonding preference of $\text{Li}-\text{F}$ over $\text{Mn}-\text{F}$, which may affect the lithium diffusion in the structure during the charge/discharge processes.²⁴ Accordingly, understanding the structural stability via fluorination, along with composition optimization, which could elucidate the lithium diffusion process limitations and ameliorate the lifetime of the battery, appears to be vital.

In this paper, we focus on the effect of fluorination and the underlying charge compensation mechanism on the structural and electrochemical properties of $\text{Li}_{1+x}\text{Mn}_{2/3}\text{Ti}_{1/3}\text{O}_2\text{F}_x$ ($0 \leq x \leq 1$) for consideration as new cobalt-free cathode materials for LIBs. Four selected compositions within the $\text{Li}-\text{Mn}-\text{Ti}-\text{O}-\text{F}$ (LMTOF) chemical system were synthesized using high-energy ball milling, characterized, and electrochemically tested. The systems are labeled according to their F/Li ratio in $\text{LiMn}_{2/3}\text{Ti}_{1/3}\text{O}_2$, $\text{Li}_{1.25}\text{Mn}_{2/3}\text{Ti}_{1/3}\text{O}_2\text{F}_{0.25}$, $\text{Li}_{1.5}\text{Mn}_{2/3}\text{Ti}_{1/3}\text{O}_2\text{F}_{0.5}$, and $\text{Li}_2\text{Mn}_{2/3}\text{Ti}_{1/3}\text{O}_2\text{F}$, hereafter referred to as 0FL, 1/3FL, 1/2FL, and 1/2FL, respectively. First, the effect of fluorination on the microstructure, morphologies, and cycling properties of the cathode materials is presented and discussed. Then, we address the structural stability according to the state of charge of the DRS cathode materials, highlighting the pioneering contribution of Raman spectroscopy to better understand Li-ion migration through a privileged percolation network.

EXPERIMENTAL SECTION

Material Synthesis. The $\text{Li}_{1+x}\text{Mn}_{2/3}\text{Ti}_{1/3}\text{O}_2\text{F}_x$ (LMTOF, $0 \leq x \leq 1$) compounds were synthesized in two steps by high-energy mechanochemical ball milling of 5 wt % excess of Li_2O (99.7%) and stoichiometric amounts of Mn_2O_3 (99%), Ti_2O_3 (99.8%), and LiF (99.9%) (all from Alfa Aesar). In the first step, the oxides were mixed together using a Fritsch P6 planetary ball mill for 20 h at 600 rpm using an 80 mL silicon nitride jar and 10 mm balls of the same material (ball-to-powder ratio, 25:1). In the second step, different amounts of LiF according to the targeted composition were added to the mixture, while the TM/O ratio was kept constant, and the powders were milled further in the same conditions as for the first step. To avoid air contamination, the synthesis procedure was carried out under an argon atmosphere.

Material Characterizations. X-ray diffraction (XRD) patterns were obtained using an airtight sample holder compatible with an STOE STADI-P diffractometer in a transmission geometry ($\text{Mo K}\alpha$ radiation, $\lambda = 0.70932 \text{ \AA}$) in a 2θ range of $10\text{--}60^\circ$ and step size of 0.02° . The crystallographic details were obtained using the Rietveld refinement method under Fullprof Suite software. VESTA software was used for visualizing the schematic illustration of crystallographic structures.

Scanning electron microscopy (SEM) and associated energy-dispersive X-ray (EDX) mappings were performed using a ZEISS GEMINI Crossbeam 350 FESEM with an in-lens detector at 5 keV equipped with an Oxford X-Max detector, using conductive carbon tape as the substrate.

For transmission electron microscopy (TEM) measurements, the samples were prepared inside an argon field glovebox and then transferred to the microscope using a vacuum transfer holder to prevent air exposure. The dry powder was directly dispersed on the TEM holey carbon membrane without the use of solvents. The measurements were performed using a Themis 300 electron microscope working at 300 kV and equipped with a DCOR probe corrector and a Super X EDX detector. The K-lines of O, F, Ti, and

Mn were used for quantification in scanning transmission electron microscopy (STEM)-EDX. STEM-electron energy loss spectroscopy (EELS) imaging was performed in a double aberration-corrected and monochromated Themis Z microscope equipped with a Gatan GIF Continuum 970 spectrometer and a K3 IS camera. The spectra were recorded with a short dwell time of only 5 ms on the K3 IS camera to reduce the influence of the beam damage on the recorded chemical state of the sample. The probe convergence angle was 30 mrad with a probe current of 200 pA. The camera length was 30 mm, and the spectrometer aperture was set to 5 mm, resulting in a collection angle of about 40 mrad.

Electrode and Cell Fabrication. To prepare a cathode film from as-synthesized compounds, 70 mg of the active compound and 20 mg of Super-P carbon black were first mixed for 3 h in an Ar-filled 20 mL silicon nitride vial with 10 balls (2 mm) as grinding media, using a Fritsch P7 planetary ball mill. The resulting composite was then mixed with poly(vinylidene fluoride) (PVDF) as a binder (10 wt %) in *N*-methyl-2-pyrrolidone (NMP) as the solvent for 15 min using a Thinky mixer (ARE-250, Thinky Inc.). The slurry was coated on an aluminum foil with an automatic doctor blade machine inside the glovebox and then dried at 120°C overnight under vacuum. Each working electrode contained ca. 2 mg of the active material. For cycling tests, Swagelok-type cells were assembled. Ethylene carbonate and diethyl carbonate (EC/DEC, 1 M LiPF_6) solution (1:1, BASF), lithium foil, and Whatman glass fiber were used as the electrolyte, counter/reference electrodes, and separator, respectively.

Electrochemical Analysis. Galvanostatic charge–discharge experiments were conducted at 25°C in a thermostatic chamber between the cutoff voltages of 1.5 and 4.3 V and at different C-rates using the Arbin BT2000 electrochemical workstation. The specific capacity was calculated based on the amount of active material in the positive electrode. Cyclic voltammetry (CV) was carried out within the voltage window of 1.5–4 V at a sweeping rate of 1 mV s^{-1} using a BioLogic VMP-3. Electrochemical impedance spectroscopy (EIS) measurements were also performed using a VMP-3 in the frequency range of 200 kHz to 1 mHz with an AC voltage of 10 mV.

Confocal Raman Microscopy and Further Characterizations.

The cathodes for ex situ Raman measurements were assembled in the same way as described above. The cells were charged and discharged at different cutoff voltages using a rate of 0.1C and allowed to stand for 12 h for equilibration. The cells were then disassembled inside the glovebox, and the LMTOF-based electrodes were separated, washed thoroughly with a DMC solvent, and then dried under vacuum for 12 h. The resulting samples were sealed between two glass slides using UHV epoxy-glue under an argon atmosphere. Raman spectra of the starting materials, Ti_2O_3 , Mn_2O_3 , and Li_2O , were collected in the spectral region $200\text{--}1000 \text{ cm}^{-1}$ using an inVia confocal Raman microscope (RENISHAW) with a 532 nm excitation laser. A grating was used as a dispersion element with a groove density of 2300 mm^{-1} , while a $50\times$ (0.75 NA) objective served as a back-scattering geometry to collect the Raman spectra. The average laser power was kept at $\sim 1 \text{ mW}$, which produced an optimal signal-to-noise ratio. To gain an average structural and surface information of the cathodes (pristine and electrochemically cycled), a surface area of $40 \times 40 \mu\text{m}^2$ was selected and a raster scan was performed with $2 \times 2 \mu\text{m}^2$ spatial resolution. To further increase the signal-to-noise ratio, the acquisition time was varied from 10 to 120 s. The cosmic rays and background were then removed from all of the spectra using Renishaw WiRETM 4.0 software. The modified Raman spectra were normalized and deconvoluted into individual spectral components using a Lorentzian line-shape function in a MATLAB programming platform.

To investigate the lithiation/delithiation process effect on the structure, ex situ XRD patterns were collected for the LMTOF-based electrodes (0FL, 1/3FL, and 1/2FL) at different charge/discharge states of the first cycle and after 50 and 100 full cycles. The electrode films were separated from the Al current collector using Kapton tape, and XRD patterns were then collected under the same conditions as described above for the raw materials. To check any solubility issue of transition metals in the electrolyte based on the proportional amount

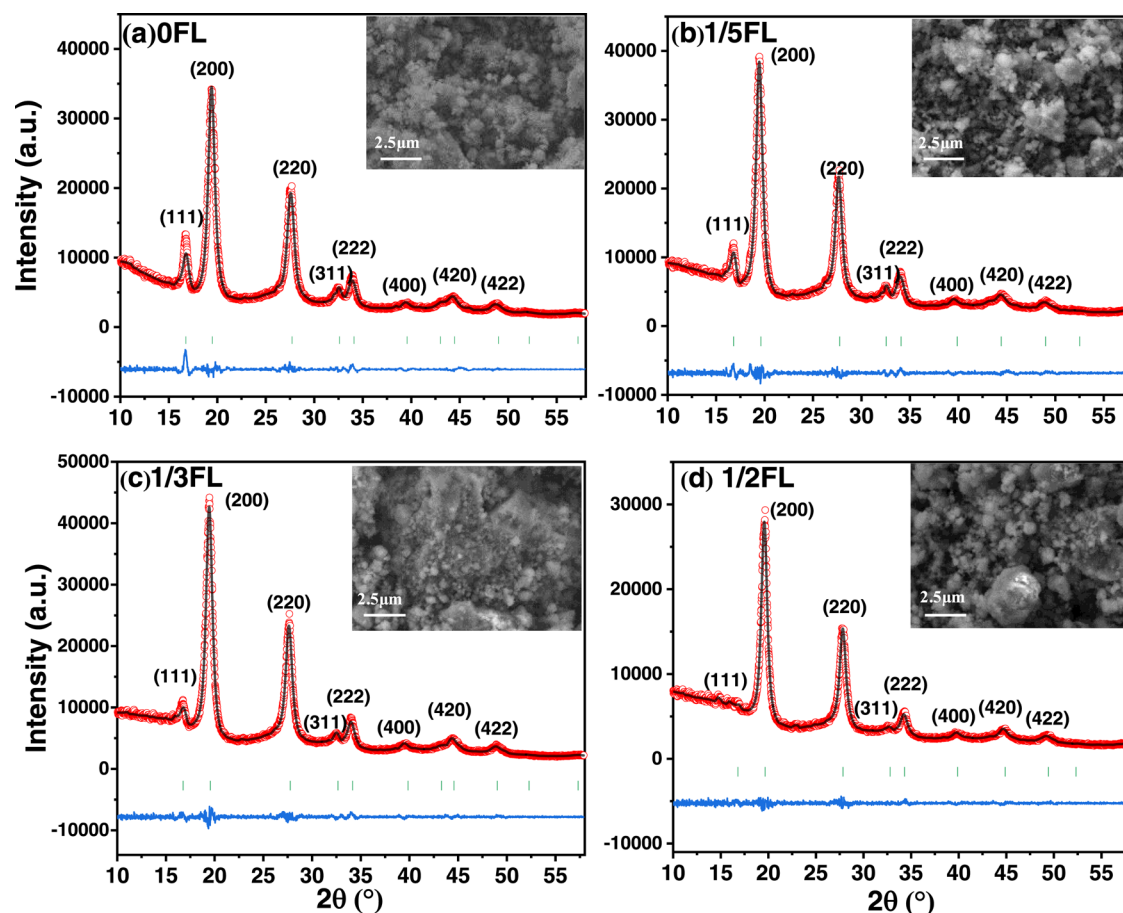


Figure 1. X-ray diffraction patterns, Rietveld refinement with a cubic rock-salt phase (space group $Fm\bar{3}m$), and the related SEM images (inset) for the samples $\text{LiMn}_{2/3}\text{Ti}_{1/3}\text{O}_2$ (0FL) (a), $\text{Li}_{1.25}\text{Mn}_{2/3}\text{Ti}_{1/3}\text{O}_2\text{F}_{0.25}$ (1/5FL) (b), $\text{Li}_{1.5}\text{Mn}_{2/3}\text{Ti}_{1/3}\text{O}_2\text{F}_{0.5}$ (1/3FL) (c), and $\text{Li}_2\text{Mn}_{2/3}\text{Ti}_{1/3}\text{O}_2\text{F}$ (1/2FL) (d), respectively, (red circles: the experimental pattern; black line: the calculated pattern; blue line: the difference plot). Bragg positions are indicated with vertical ticks.

of Mn and Ti, which could come out of the structure, inductively coupled plasma-optical emission spectroscopy (ICP-OES) analysis was conducted for the lithium foil counter electrode of the cells after 50 and 100 cycles. The Li foil samples were dissolved overnight in concentrated aqua regia until complete dissolution before they were subjected to ICP-OES sampling and analysis.

RESULTS AND DISCUSSION

Characterization of the Synthesized Materials. Figure 1 shows the XRD patterns of the successfully synthesized compounds $\text{LiMn}_{2/3}\text{Ti}_{1/3}\text{O}_2$ (0FL), $\text{Li}_{1.25}\text{Mn}_{2/3}\text{Ti}_{1/3}\text{O}_2\text{F}_{0.25}$ (1/5FL), $\text{Li}_{1.5}\text{Mn}_{2/3}\text{Ti}_{1/3}\text{O}_2\text{F}_{0.5}$ (1/3FL), and $\text{Li}_2\text{Mn}_{2/3}\text{Ti}_{1/3}\text{O}_2\text{F}$ (1/2FL). In the four cases, Rietveld refinement analysis confirms the formation of the single-phase disordered rock salt structure with the space group $Fm\bar{3}m$ with no observable impurity or precursor peaks. On increasing fluorine substitution (Table 1), the lattice constant slightly decreases from 4.216 Å (0FL) to 4.179 Å (1/2FL). This decrease is a result of higher differences of electronegativity between fluorine and oxygen atoms, which lead to shorter bonds and thus a smaller lattice constant.²⁵ The detailed data of the refinements are presented in Table S1 of the Supporting Information (SI) file. Additionally, it can be observed that the intensity of the (111) reflection with respect to (200), I_{111}/I_{200} , diminishes upon fluorination, which is related to a lithium-rich plane of the reciprocal space. This result is a further hint that LiF added in

Table 1. Structural Parameters of the Different Phases Based on Rietveld Refinement and SEM Analysis

composition	lattice parameter (Å)	cell volume (Å ³)	crystallite size (nm)	av. particle size (nm)
$\text{LiMn}_{2/3}\text{Ti}_{1/3}\text{O}_2$ (0FL)	4.216(2)	74.95(2)	5 ± 1	207
$\text{Li}_{1.25}\text{Mn}_{2/3}\text{Ti}_{1/3}\text{O}_2\text{F}_{0.25}$ (1/5FL)	4.208(2)	74.52(4)	6 ± 1	237
$\text{Li}_{1.5}\text{Mn}_{2/3}\text{Ti}_{1/3}\text{O}_2\text{F}_{0.5}$ (1/3FL)	4.206(1)	74.38(1)	7 ± 2	297
$\text{Li}_2\text{Mn}_{2/3}\text{Ti}_{1/3}\text{O}_2\text{F}$ (1/2FL)	4.179(2)	71.94(2)	8 ± 2	280

the second stage of synthesis is successfully incorporated in the DRS structure.

The nano-sized nature of the phases can be expected according to the broadening of the reflection peaks.^{26,27} Using the Williamson–Hall method (Table 1), the crystallite size increases slightly on increasing the amount of fluorine from 5.7 nm (0FL) to 7.2 nm (1/2FL). In general, the dry ball milling process often induces significant strain in the particles, where the average lattice microstrain was calculated to be <0.5% for all of the samples.²⁸ Figure S1 shows the one-dimensional (1D) view comparison of the XRD patterns by increasing the amount of fluorine. All of the main peaks reveal a visible shift

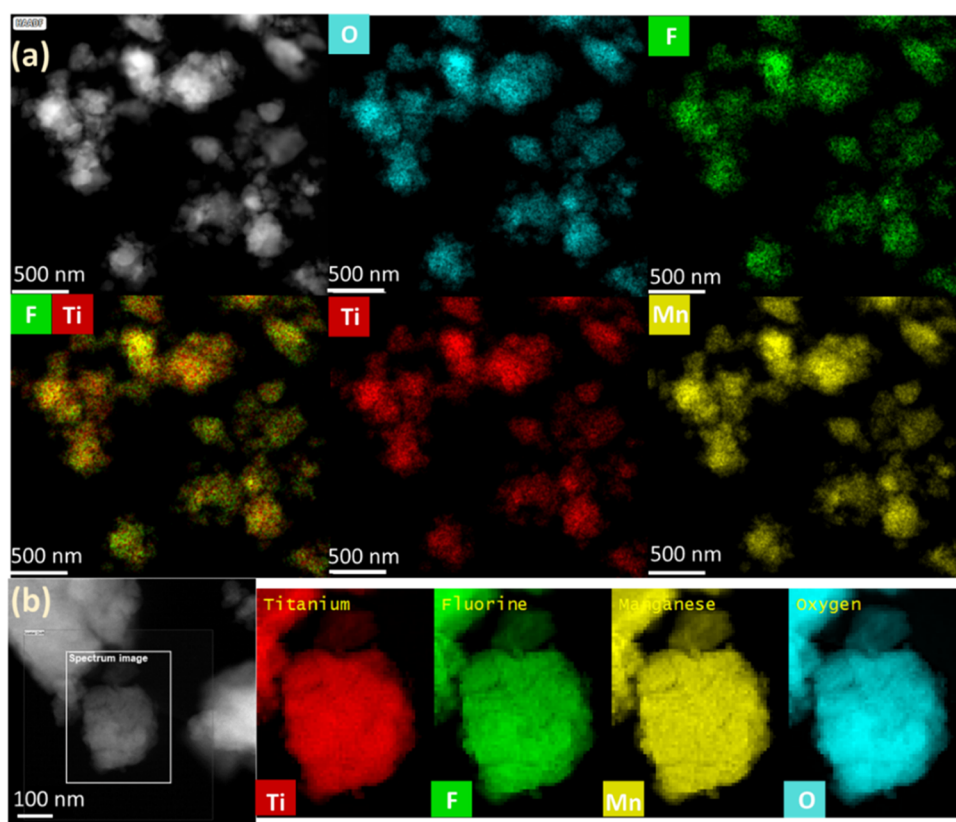


Figure 2. (a) EDX mapping with a large field of view and (b) EELS mapping using a core loss region for the 1/2FL sample.

to higher angles, which is in agreement with the crystal lattice shrinking driven from Rietveld refinement.

Characterization of the powder samples by SEM indicates a quasispherical morphology of the particles after a mechanical milling process (insets in Figure 1). As observed in the images, the average particle size of the as-synthesized materials lies in the range of $\approx 207\text{--}280$ nm (Table 1). However, the images also reveal agglomeration of primary particles into secondary particles, which are around ≈ 1 μm in size as a result of aggregation of the powder after ball milling. Since no significant LiF can be observed in the XRD patterns, we used SEM-EDX chemical mapping (Figure S2) to track locally whether all of the fluorine was incorporated in the structure rather than remaining as a LiF impurity (single-phase or particle surface coating). The results reveal a uniform and homogeneous distribution of fluorine in the three fluorine-containing samples (1/5FL, 1/3FL, and 1/2FL), along with the other elements, since there are no titanium- or manganese-rich areas visible on the mapping. Based on these observations and the discussed XRD pattern evolution upon fluorination, we assume that the fluorine was successfully incorporated into the compounds. Furthermore, the elemental composition derived from EDX measurements corroborates the expected composition for the four samples. The detailed elemental analysis is available in Table S2 (SI).

EDX mapping with a large field of view (Figure 2a) and EELS-based elemental mapping (Figure 2b) for the 1/2FL sample present a homogeneous distribution of the elements and do not show any detectable fluoride distribution outside the DRS structure. EELS spectra of the Mn L-edge, Ti L-edge, F K-edge, and O K-edge on the surface and bulk were collected to define the oxidation states of the transition metals. As shown

in Figure S3, Mn L-edge did not show distinct energy positions and shapes between the surface and center. Here, representative spectra of the center of the particle were added. The energy position at 641.5 eV is higher than that expected for Mn^{II} , but the $L3/L2$ ratio in the range of 2.5 is specific for the $\text{Mn}^{\text{III}}/\text{Mn}^{\text{II}}$ mixture. The energy position is sensitive to the chemical environment, and so the shift to higher energy can be explained. Both the fine structure and the energy loss position of the Ti L-edge show a Ti^{4+} oxidation state, and no change between the surface and the bulk (center) of the nanoparticles can be observed. Oxygen K-edge shows a fine structure specific for Ti^{4+} ; however, this could be influenced by the presence of fluorine and the highly disordered Mn–Ti mixed cations. The Li K-edge shows a similar fine structure and energy position as other studies on cathode materials. We can conclude that this observation, together with the fact that in the high field view of EDX mapping no F surrounding the particles could be identified, is additional proof for the F insertion inside the structure.

Electrochemical Characterization and Postmortem Analysis. The galvanostatic (de)lithiation voltage profiles of the samples with different fluorine contents (1/5FL, 1/3FL, and 1/2FL) after 1st, 3rd, 10th, and 100th cycles are presented in Figure 3a. During the first cycle, the 1/5FL-, 1/3FL-, and 1/2FL-based electrodes delivered initial discharge capacities of 232 mAh g^{-1} (67% theoretical capacity), 212 mAh g^{-1} (55% theoretical capacity), and 248 mAh g^{-1} (54% theoretical capacity), respectively, based on a two-electron redox of Mn ions. The higher initial reversible capacity of the 1/5FL sample observed could be attributed to its lower fluorine content, allowing the extraction of more lithium.²⁹ However, on increasing the amount of fluorine, the lithium content also

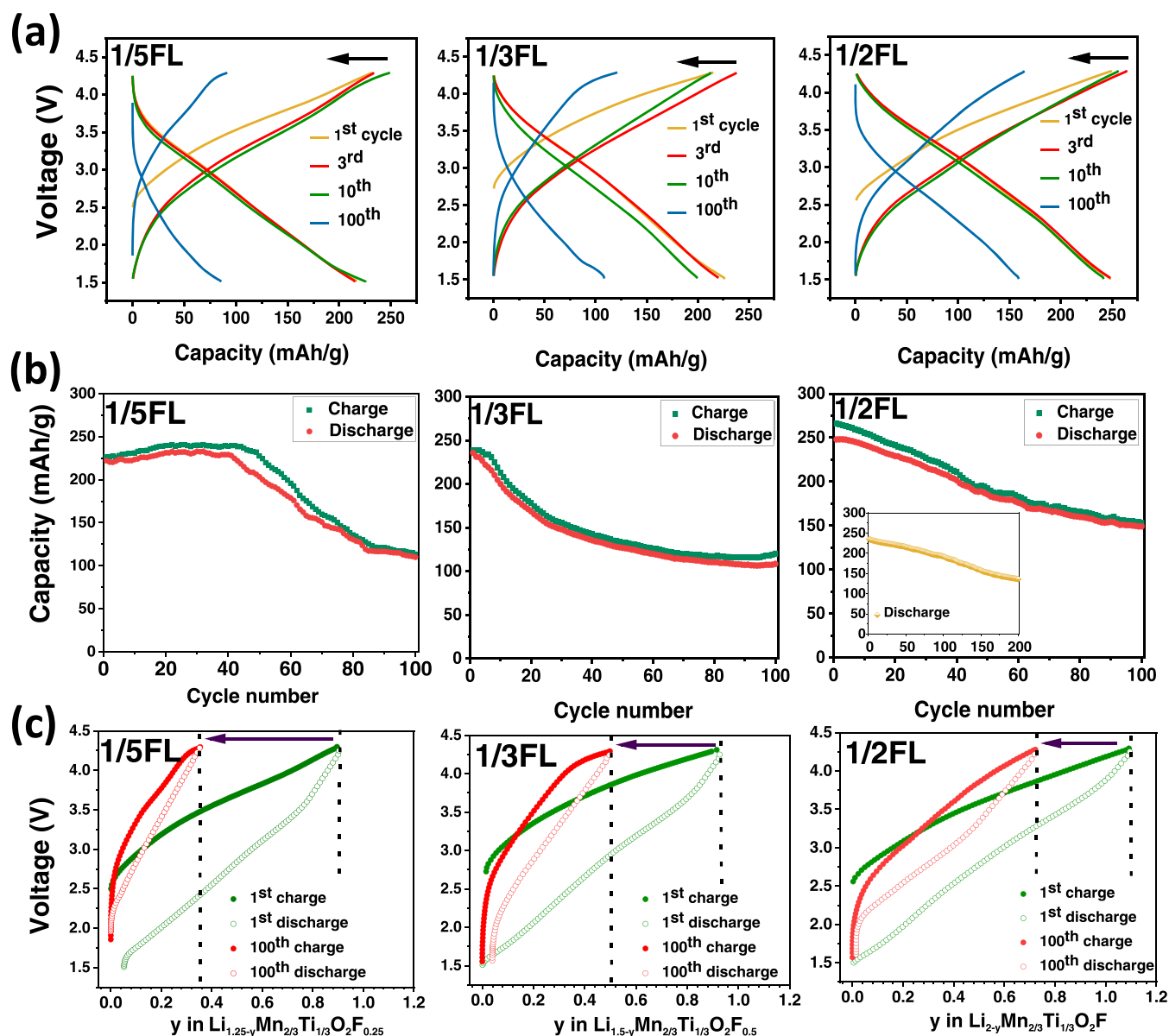


Figure 3. Voltage profiles (a) for 1st, 3rd, 10th, and 100th cycles of the three fluorinated samples 1/5FL, 1/3FL, and 1/2FL. The corresponding capacity retention (b) as a function of cycle number and specific circle plots (c) of the voltage versus $y(\text{Li}^+)$ after first and 100th cycles (25 °C and 4.3–1.5 V at a C-rate of 0.1C).

increased in the structure, which led to a higher initial discharge capacity. In the case of a cation DRS system, a volume change during the lithiation process is believed to occur in an isotropic manner, which potentially would reflect the fraction of lithium ions involved in the reversible electrochemical cycling.³⁰ Therefore, high-capacity electrode materials consistent with a long cycle life can be anticipated. The voltage profile of the samples shows a sloping behavior both during lithiation and delithiation without any obvious plateaus, which suggests a single-phase process. In comparison to other samples, the 1/2FL sample showed a more sloping profile during cycling. In such a system, any change in the voltage profile can be correlated with the stoichiometry of the active material.³¹ The galvanostatic (de)lithiation voltage profiles and the corresponding capacity retention plot of the OFL sample are shown in Figure S4. It should be noted that this study is focused on F-containing materials and their cycling properties, where the comparison with non-fluorinated

samples becomes tricky owing to the strong Li–F interaction. Figure 3b shows that after 10 cycles, all of the samples exhibit good reversibility and capacity retention. The discharge capacities are situated around 93, 109, and 160 mAh g⁻¹ after 100 cycles for 1/5FL, 1/3FL, and 1/2FL samples, respectively. It is worth mentioning that the 1/2FL sample showed about 130 mAh g⁻¹ discharge capacity after 200 cycles, corresponding to ~61% of the initial capacity (inset in Figure 3b).

The capacity loss of the samples during cycling could be related to oxygen loss, which may occur at high voltages. The O-redox activity leading to higher capacities is assumed to be followed by the dissolution of a certain amount of Mn in the electrolyte. The abovementioned process would result in destabilizing the structure, which could lead to significant electrode degradations. However, fluorination seems to alleviate these irreversible anionic reactions.²⁵ In fact, fluorination stabilizes the electrode/electrolyte interface,

leading to a higher cycle life of the battery.³² The discharge capacity differences between the samples increase with the cycle number, mainly after 40 cycles.

Figure 3c shows the voltage profile as a function of active lithium. It reveals that the observed high discharge capacity during the first cycle is associated with continuous lattice volume expansion upon lithium insertion. Thus, approximately 0.91, 0.93, and 1.1 Li⁺ per TM can be cycled, respectively, for 1/5FL, 1/3FL, and 1/2 FL samples. However, these amounts decreased to 0.35, 0.5, and 0.73 Li⁺ after 100 cycles. These values show the accessible capacity for the active material in comparison to the theoretical capacity assuming a stoichiometric amount of Li⁺.¹⁸ By comparing the amounts after 100 cycles, the 1/2FL sample showed the highest amount of y , which is a sign of better cyclability.

In the case of cathodes suffering from TM dissolution issues, it has been similarly reported that high C-rates would show better capacity retention.³³ This is particularly due to a less interaction time of the active material with the electrolyte.³⁴ To investigate how fast the compounds would react to the changes in the current rate, we cycled all three compounds under the same voltage profile (1.5–4.3 V) at different C-rates from 0.1C to 1C and back to 0.1C (Figure 4). The particular nanostructure and morphology of the samples, clarified by STEM imaging, are proposed to be responsible for the acceptable rate capability of the samples. At a low C-rate (0.1C), all samples exhibited slightly different discharge capacities. However, at a high C-rate (1C), the discharge capacities of the 1/2FL sample were significantly higher around 200 mAh g⁻¹ than the other two samples (around 130 mAh g⁻¹). The improved rate capability, which can be seen for highly fluorinated samples, originates from a drastic reduction of electrode impedance (Figure S6), as discussed below. The samples also show good capacity retention with high average Coulombic efficiency (CE) (>90%) when the current rate goes back to 0.1C. The results based on the Coulombic efficiency in all of the rates stipulate that the capacity loss, presumably via Mn dissolution, occurred during the delithiation process.

To investigate the Mn dissolution further, ICP-OES analysis was done for the fluorinated samples (1/5FL, 1/3FL, and 1/2FL) on the collected lithium foil from half-cells after 50 and 100 cycles. The aim is to get more information on the approximate amount of Mn and Ti, which could result from the structure and deposit on the Li foil by ion migration; doing so, a link to the chemical stability under voltage sollicitation can be established. The analytical results (Table S3) plotted in Figure 5a,b show a higher concentration of Mn, around 10 times higher than that of Ti, in all of the samples, which is proof of manganese stability in the structure.³⁵ It can be deduced that by increasing the amount of fluorine, the amount of detected transition metals on the lithium foil decreases. This trend is confirmed by cycling for 100 cycles. The results approve that one of the reasons behind capacity loss during cycling is related to the instability of the active Mn in the structure.³⁶ Consequently, fluorination seems to play a key role in attenuating Mn dissolution and structure stabilization.

The dQ/dV curves were calculated to evaluate the influence of fluorine on the redox mechanism of the three samples (1/5FL, 1/3FL, and 1/2FL) during cycling (Figure S5a). All of the samples showed two redox processes, where two equilibrium potentials can be identified at around 2.5 and 3.4 V, assigned, respectively, to the Mn^{III}/Mn^{II} and Mn^{IV}/Mn^{III} redox couples. The 1/5FL sample, in comparison to the two

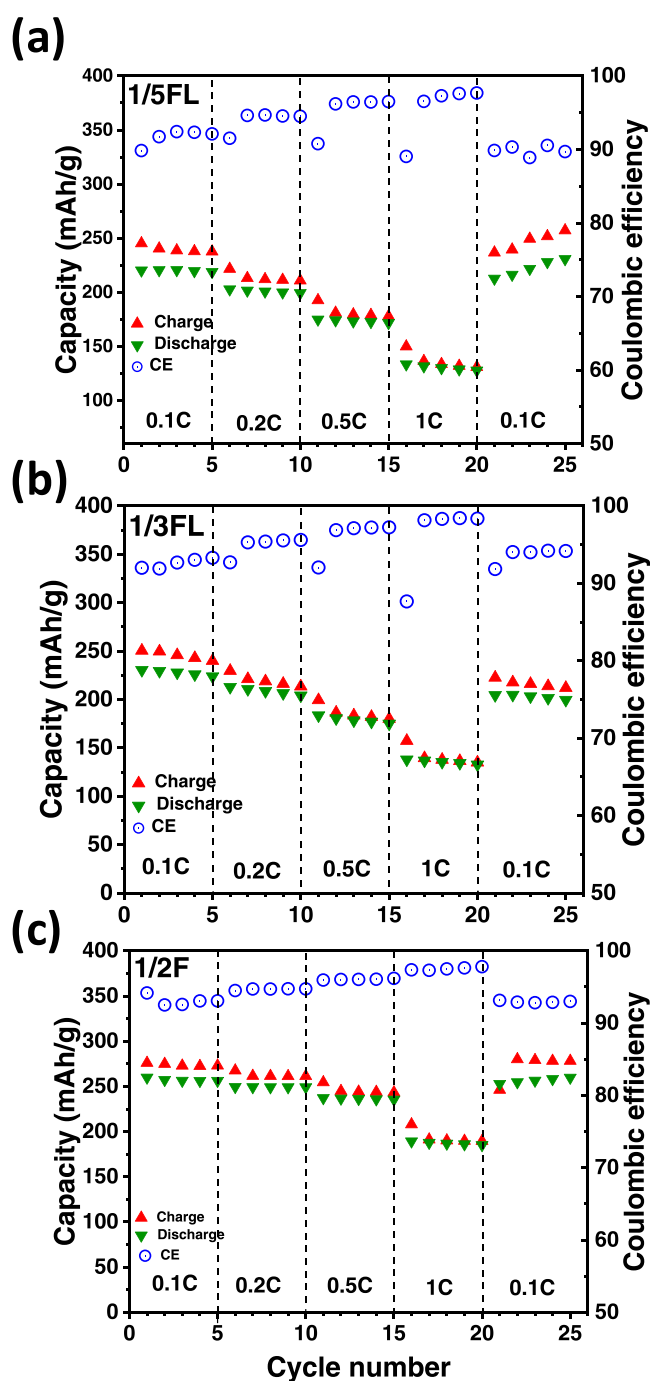


Figure 4. Rate capability comparison of the three fluorinated samples, 1/5FL (a), 1/3FL (b), and 1/2FL (c), respectively, within the voltage window of 1.5–4.3 V at 25 °C. Coulombic efficiency (CE) is given on the right Y-axis.

other samples, exhibits the sharpest peaks at both redox reactions, which justifies the high capacity with respect to the theoretical one. The observed deviations between the charge/discharge peak locations for the samples witnesses the differences in the reversibility of the processes. This behavior can be influenced by polarization and kinetic effects according to differences in the composition of the samples. One possible mechanism that should be mentioned is that increased polarization can reduce the amount of charge transferred and cycle reversibility in the region of overpotential.³⁷ Furthermore, by comparing the overpotentials in different samples, a

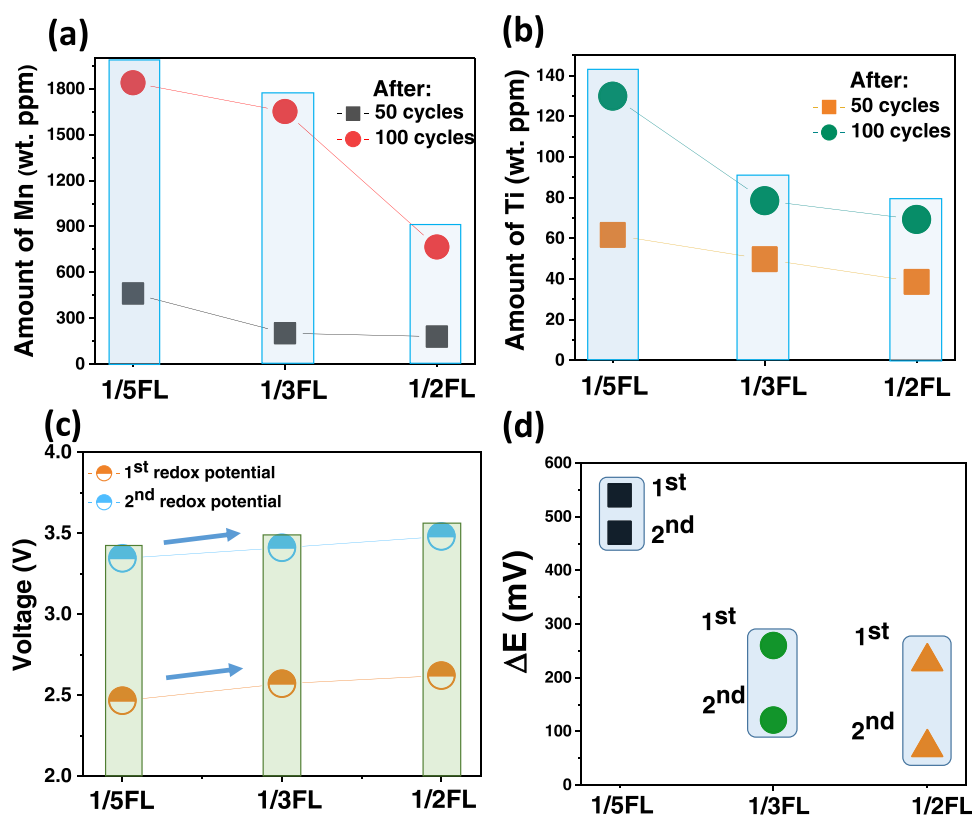


Figure 5. Manganese (a) and titanium (b) amounts (wt ppm) on the lithium foil anode determined from ICP-OES analysis. Comparison of the first and second Mn redox potentials (c) extracted from the average voltages of dQ/dV and CV plots for the three fluorinated samples (1/5FL, 1/3FL, and 1/2FL) at a scan rate of 0.5 mV s^{-1} . Evolution of the differences (d) between reduction and oxidation voltages upon fluorination during CV scans (first redox $\text{Mn}^{\text{II}}-\text{Mn}^{\text{III}}$; second redox $\text{Mn}^{\text{III}}-\text{Mn}^{\text{IV}}$).

relation between the redox voltage and the composition of the samples can be elucidated.³⁸ The voltage of the first redox reaction increased from around 2.4 V for the 1/5FL sample to 2.6 V for the 1/2FL sample, and the voltage of the second redox reaction increased from around 3.3 V for 1/5FL sample to 3.5 V for the 1/2FL sample. These results confirm clearly the structural effect of fluorine substitution on the electrochemical reactions.

Independently, Figure S5b shows the CV curves of the three compounds and compares them to 0FL, which confirms the redox processes obtained from dQ/dV analysis. Figure 5c,d shows the average voltages of the redox process of the three fluorinated samples extracted from both dQ/dV and CV curves. In fact, by increasing the amount of fluorine, the oxidation peaks move to higher potentials, which demonstrates that fluorine exerts an effect on the free energy of the compounds (Figure 5c) and hence the improved thermodynamic stability. Furthermore, the 1/2FL sample shows the smallest voltage deviation between oxidation and reduction (Figure 5d). By increasing the amount of fluorine, the reversibility yield has been increased, indicating a stable and well-defined Li^+ diffusion mechanism.³²

EIS spectra were recorded to extract the characteristic kinetic parameters such as the charge and mass transfer resistances ($R_{\text{ct}} + R_{\text{mt}}$), which can be defined from the length of the main semicircle. The bulk resistance can be inferred from the starting of the main semicircle, for 1/5FL, 1/3FL, and 1/2FL samples, for the initial fresh cell and after each cycle (to 4.3 V) and discharge (to 1.5 V) of the first 50 cycles. Figure S6 shows the variation of the total resistance during lithiation and

delithiation for the fresh cells and after the 1st, 10th, 30th, 40th, and 50th cycles. All of the materials show similar starting points and display growth in impedance, mainly after 10 cycles. The initial R_{ct} values for the three electrodes were 209, 540, and 290 Ω , which increased to around 611, 1460, and 1200 Ω after the 50th cycle, respectively, for 1/5FL, 1/3FL, and 1/2FL samples. The semicircles become larger in the fully lithiated than delithiated electrodes during all of the cycles, which is due to stoichiometric differences. Also, it can be inferred that the electrodes in the discharged mode have faster kinetics. The R_{ct} increase with cycling is attributed to significant changes in the electrode surface.³⁹ However, the increase in impedance with cycling is in accordance with the continuous capacity fading seen from the electrochemical results. The 1/2FL sample showed the smallest resistance in all cycles and after 50 cycles. This can be attributed to more stable structures and dynamics. These observations suggest that the microscopic lithium-ion diffusion behavior can be largely different due to differences in atomic configuration and repulsion energies around each cation, chemically influenced by the presence of fluorine.⁴⁰

For a better understanding of the electrochemical behavior and cycling stability of the materials on changing the fluorine content, ex situ X-ray diffraction was conducted at different cutoff voltages during charge and discharge and after prolonged cycling (50–100 cycles). Figure 6 shows the comparison of the XRD patterns at different charge/discharge states and cycle numbers for the 1/2FL sample. It can be seen that the intense peak observed at a low angle in all of the patterns corresponds to the (200) reflection of the DRS structure. The peak shift reflects the change in the lattice

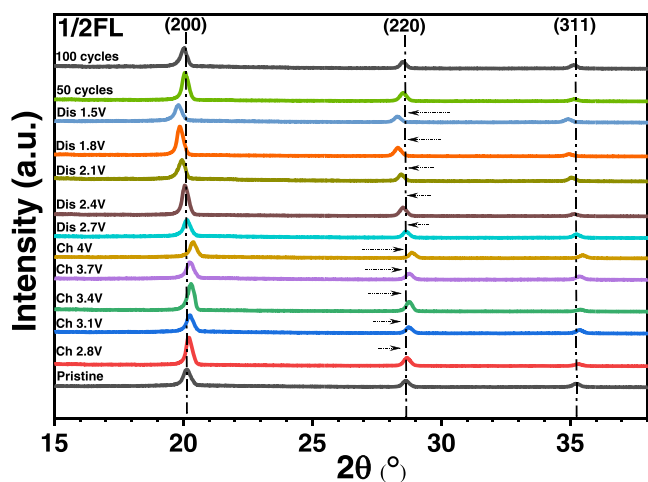


Figure 6. Ex situ XRD patterns of the 1/2FL sample at different stages of charge and discharge and after 50 and 100 full cycles (discharged state).

parameter upon the Li^+ (de)insertion. By charging (delithiation) the cell from 2.8 to 4 V, the peaks shift slightly to higher angles, which correspond to smaller lattice parameters. Interestingly, as the discharge (lithiation) proceeds from 4 V down to 1.5 V, the peaks revert reversibly back to lower angles, which demonstrates the good DRS structure stability during lattice shrinking/expansion. On further cycling of the electrodes for 50 and 100 cycles, the XRD patterns were found to be similar to the pattern of the initial electrode with no obvious

extra peaks, which is a priori an indication that no significant phase transition or side reaction occurred during the 100th cycle. These observations confirm the apparent stability of the electrode materials and approve the proper cycling performance in the voltage range of 1.5–4 V. The same trend was observed for the other two samples, 0FL and 1/3FL (Figure S7), except that peak shifts are significantly pronounced for 0FL, confirming the beneficial effect of F to minimize the lattice expansion during operational conditions.

Raman Spectroscopy of Pristine and Cycled LMTOF Materials. To complement the XRD limitations, Raman spectroscopy is a highly sensitive technique to identify minute structural and coordination changes. Fluorine incorporation, as well as successive (de)lithiation processes, can have profound effects on the DRS structural network, and changes in the coordination can be identified by Raman spectroscopy. For the $Fm\bar{3}m$ space group, considering a composition without F, cations are octahedrally coordinated with an oxygen cubic closed packed network (MX_6). The MX_6 moiety can be represented by the O_h^5 symmetry,^{41,42} and there are four Raman-active modes, which can be represented as

$$\Gamma_{Fm\bar{3}m} = A_{1g}(R) + E_g(R) + 2F_{2g}(R)$$

The pictorial representation of the A_{1g} , doubly degenerate E_g , and one of the triply degenerate F_{2g} modes is shown in Figure 7a, which are involved with only oxygen motion. Additionally, the second F_{2g} mode implies the motion of the whole MX_6 moiety with respect to a neighboring cation,⁴³ which is not represented here.

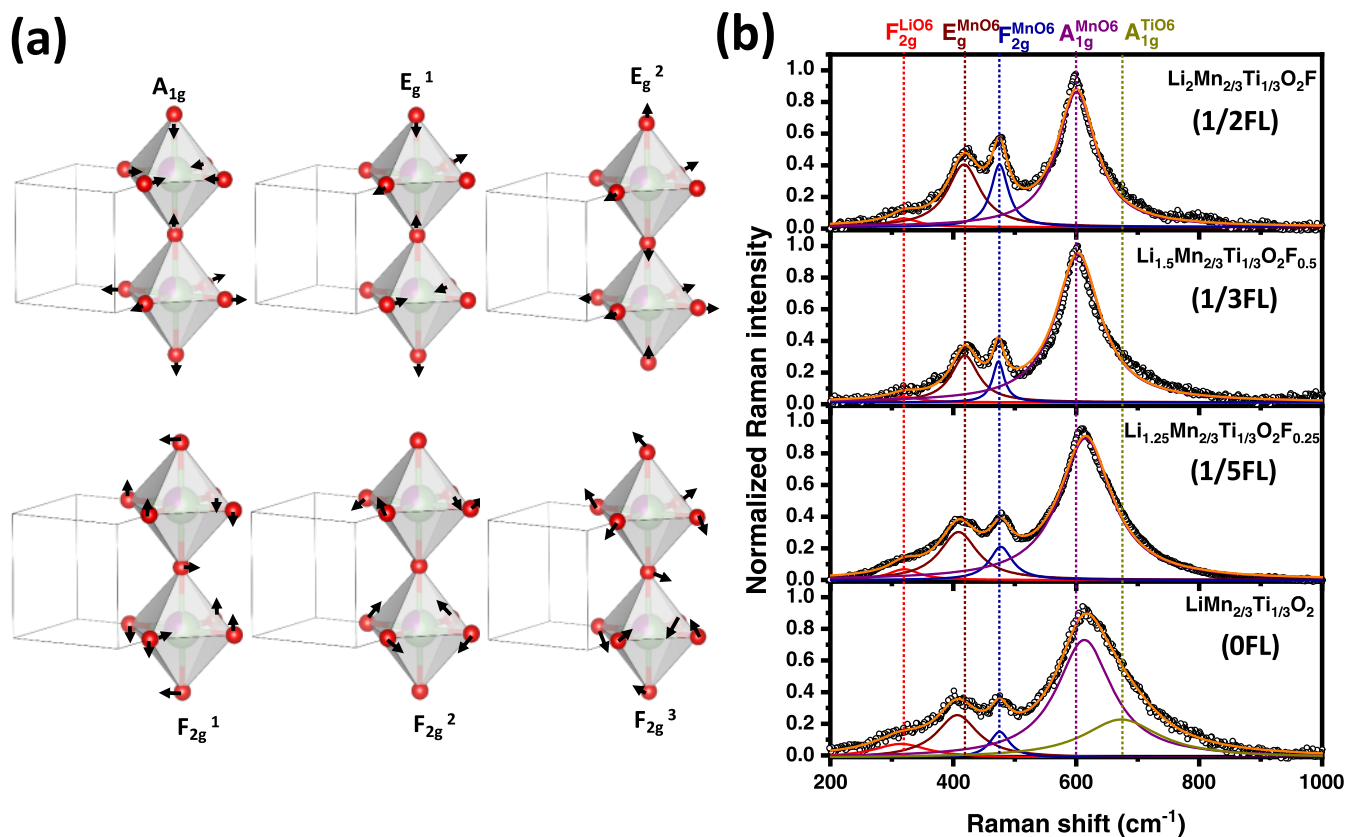


Figure 7. Selected Raman normal modes (a) allowed for the $Fm\bar{3}m$ structure. Green, purple, and red represent, respectively, Li ions, TMs (Mn/Ti), and anions (O/F). Raman spectra (b) of the different pristine materials (OFL, 1/5FL, 1/3FL, and 1/2FL). The respective deconvoluted bands are also represented, which are reminiscent of the $Fm\bar{3}m$ structure.

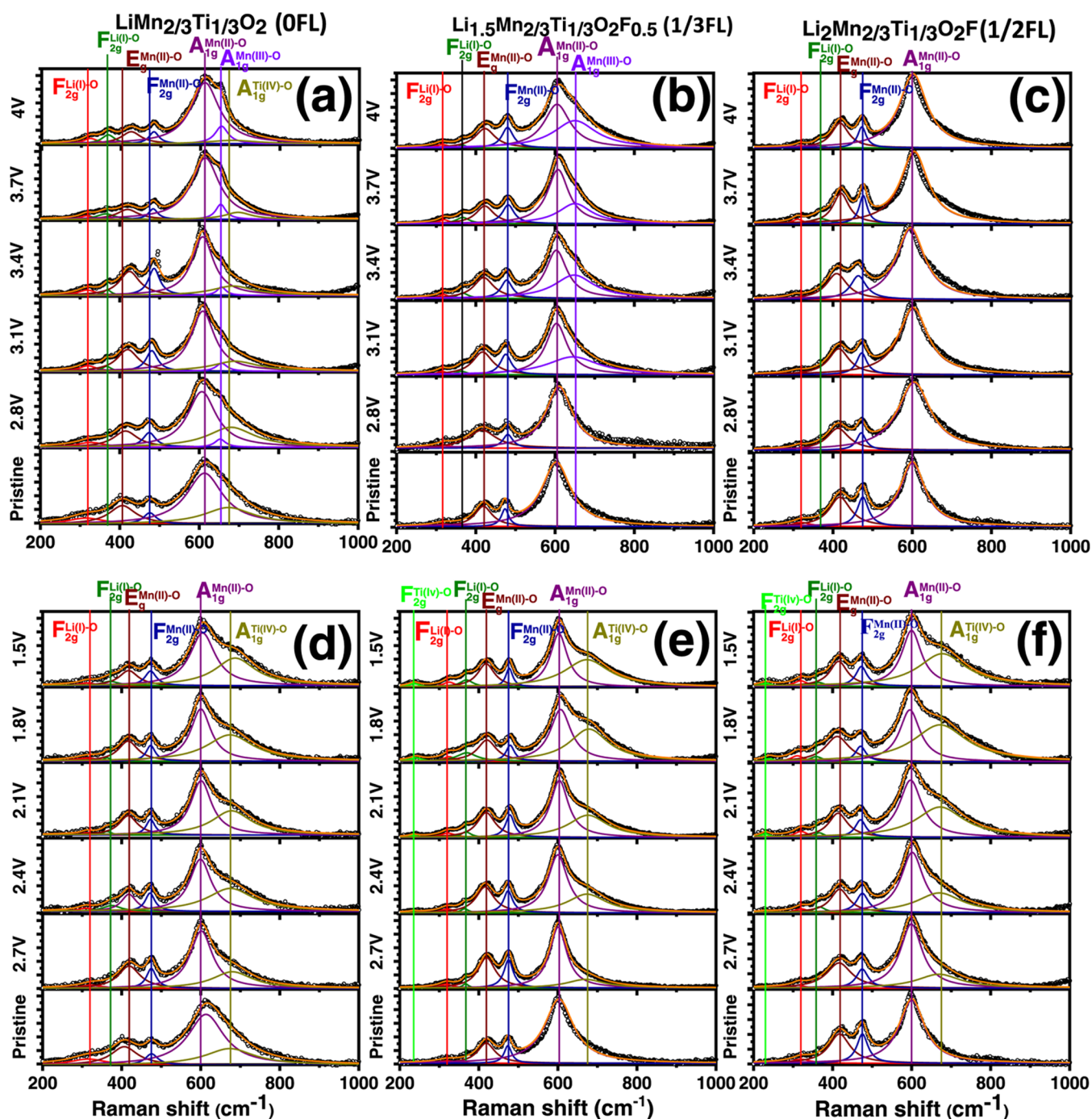


Figure 8. Normalized Raman spectra with deconvolution of respective vibrational bands at different final charged (a–c) and discharged (d–f) states, respectively, for 0FL-, 1/3FL-, and 1/2FL-based cathodes.

Pristine Materials. The Raman spectrum (Figure 7b) of the 0FL sample can be resolved into five bands corresponding to five different vibrations present in the crystal lattice. The bands at 615, 475, and 406 cm^{-1} are primarily attributed to A_{1g} (out-of-plane symmetric stretching), F_{2g} (bending), and E_g (asymmetric stretching) of the $\text{Mn}^{\text{II}}\text{O}_6$ octahedra, respectively.^{44–46} The second F_{2g} mode of the $\text{Mn}^{\text{II}}\text{O}_6$ octahedra is below 200 cm^{-1} and out of our detection region. The peak at 673 cm^{-1} is assigned to the symmetric A_{1g} stretching of $\text{Ti}^{\text{IV}}\text{O}_6$ octahedra,^{47,48} whereas the poorly resolved band at 314 cm^{-1} arises from the bending F_{2g} mode of $\text{Li}^{\text{I}}\text{O}_6$ octahedra.⁴⁸ These fingerprints in the 0FL Raman spectrum guide our under-

standing that although the material is disordered, there are different amounts of local ordering present in $\text{Mn}^{\text{II}}\text{O}_6$, $\text{Ti}^{\text{IV}}\text{O}_6$, and $\text{Li}^{\text{I}}\text{O}_6$ octahedral structures. All of these bands are broad, indicate a significantly low local ordering, and are reminiscent of ball-milled powders with substantial nanocrystallinity. These identified features do change to different extents, as the fluorine is incorporated into the structure (Figure 7b), where the band at 673 cm^{-1} (A_{1g} of $\text{Ti}^{\text{IV}}\text{O}_6$ octahedra) vanishes. In addition, the increase in the total fluorine stoichiometry leads to the narrowing of the dominant stretching A_{1g} vibrational band of $\text{Mn}^{\text{II}}\text{O}_6$ and the associated relative increment of the F_{2g} bending vibration mode (Figure S9b). It was found that the

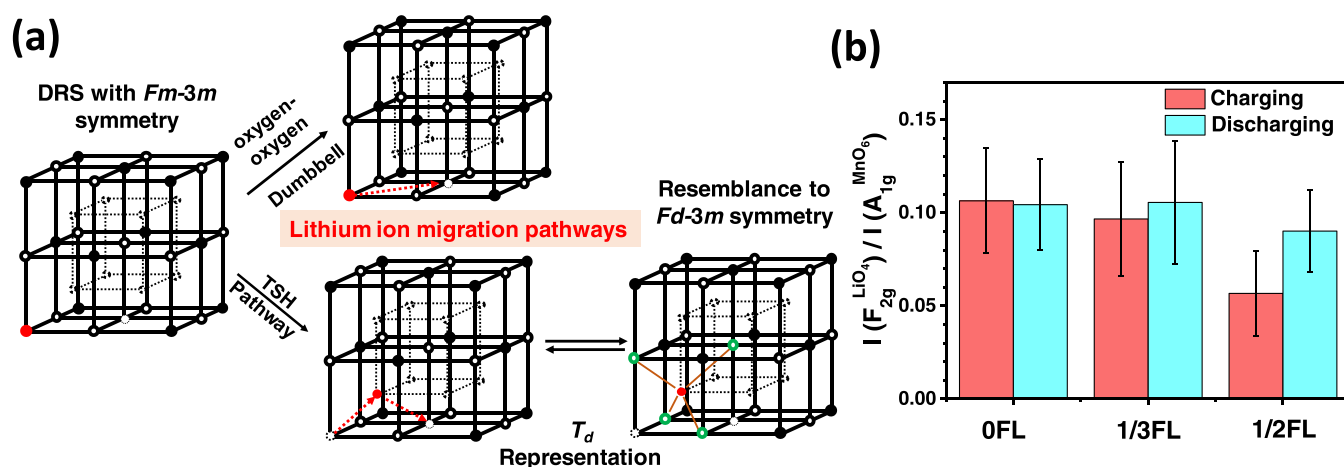


Figure 9. Pictorial representation (a) of a possible Li^+ migration path throughout the crystal lattice. The average intensity ratio of the (b) $F_{2g}(\text{Li}^1\text{O}_4)$ band with respect to the $A_{1g}(\text{Mn}^{\text{II}}\text{O}_6)$ band as a function of the amount of substituted fluorine in the cathode materials during charging and discharging.

substituent fluorine anions in the LMTOF system preferentially coordinate with Li^+ and Ti^{IV} ions rather than with Mn^{II} . As the stoichiometry of fluorine increases, the enhancement of the short-range local ordering in $\text{Mn}^{\text{II}}\text{O}_6$ octahedra occurs. The peak frequency of the symmetric A_{1g} band of $\text{Mn}^{\text{II}}\text{O}_6$ in 0FL is higher than that of 1/2FL by 10 cm^{-1} (Figure S9a), indicating that the terminal oxide anions are strongly bound to $\text{Ti}^{\text{IV}}/\text{Li}^+$ in 0FL, which strengthens the above statement.^{49,50}

Monitoring charge and discharge of the cathodes by ex situ Raman spectroscopy measurements can be of relevant input to gain insight into structural and reaction mechanisms involved in the electrochemical process. To figure out the possible effect imposed by the fluorination, three cathode materials, 0FL, 1/3FL, and 1/2FL have been selected. The Raman spectra were collected at five different charged and discharged potential states. Figure 8 shows the normalized spectra from electrodes at different cutoff voltages during the first cycle and compared to pristine electrodes (uncycled). The spectra represented here are averaged over several points and found to be reproducible across different surface regions of the cathodes.

Delithiated Cathodes. In the case of 0FL, deconvoluted spectra (Figure 8a) show the presence of all of the recognizable Raman bands $A_{1g}(\text{Ti}^{\text{IV}}\text{O}_6)$, $A_{1g}(\text{Mn}^{\text{II}}\text{O}_6)$, $F_{2g}(\text{Mn}^{\text{II}}\text{O}_6)$, $E_g(\text{Mn}^{\text{II}}\text{O}_6)$, and $F_{2g}(\text{Li}^1\text{O}_4)$, which have been discussed above. Upon delithiation, two new bands appear at 367 cm^{-1} and 652 cm^{-1} , which shed light on the change in the lattice structure and reaction pathways in the F-free material. The spectral band near $\sim 650\text{ cm}^{-1}$ is the signature of the A_{1g} symmetric vibration of the $\text{Mn}^{\text{III}}\text{O}_6$ octahedra.⁵¹ This band frequency matches with the intense peak of the starting precursor Mn_2O_3 , which is due to $\text{Mn}^{\text{III}}\text{--O}$ stretching (Figure S8a). Note that with continuous delithiation, the relative intensity of the $A_{1g}(\text{Mn}^{\text{III}}\text{O}_6)$ band increases and the band width decreases. The charge balance in the system is preserved by the $\text{Mn}^{\text{II}}\text{--Mn}^{\text{III}}$ oxidation reaction. The $A_{1g}(\text{Ti}^{\text{IV}}\text{O}_6)$ band becomes vanishingly small, and the peak position shifts toward a higher frequency. This shift indicates that the delithiation occurs from the neighborhood of the $\text{Ti}^{\text{IV}}\text{O}_6$ cage and, in turn, makes the $\text{Ti}^{\text{IV}}\text{--O}$ bond shorter. The disappearance of the $A_{1g}(\text{Ti}^{\text{IV}}\text{O}_6)$ mode correlates to the decreased short-range ordering of the $\text{Ti}^{\text{IV}}\text{O}_6$ octahedra as the delithiation reaches a penultimate stage. The ordering in the $\text{Ti}^{\text{IV}}\text{O}_6$ and $\text{Mn}^{\text{II}}\text{O}_6$ moieties is interlinked and partially stabilized by shared

coordination with lithium. As the lithium leaches out of the crystal lattice, the local ordering is hampered. The $E_g(\text{Mn}^{\text{II}}\text{O}_6)$ and $F_{2g}(\text{Mn}^{\text{II}}\text{O}_6)$ bands also experience a blue shift upon delithiation (Figure S10), mainly for the bending mode, suggesting a shortened $\text{O--Mn}^{\text{II}}\text{--O}$ bond angle in the $\text{Mn}^{\text{II}}\text{O}_6$ octahedron.

The new low-frequency band at $\sim 370\text{ cm}^{-1}$ (Figure 8a) is attributed to the F_{2g}^3 bending vibration of the Li^1O_4 tetrahedral moiety.⁴⁸ This band appears due to the trapping of the lithium ions in the tetrahedral sites, reminding the $Fm\bar{3}m$ symmetry (spinel-type lattice).⁵² The absence of any signature from the tetrahedral coordination from TMs in the deconvoluted Raman spectra provides evidence that the delithiation procedure is carried out through this low-strain structural change, where only lithium moves from site to site. The appearance of this Li^1O_4 bending mode sheds light on the plausible Li^+ migration mechanism. Lithium diffusion in an octahedrally coordinated lattice is generally accepted to occur in two distinct pathways, tetrahedral sight hops (TSH) and oxygen-oxygen dumbbell hops.^{15,53} In the TSH mechanism, lithium ions move from an octahedron site to an adjacent vacant octahedron site via passing through a tetrahedron site (Figure 9a). On the other hand, lithium ions can forcefully translate between two adjacent octahedral sites through the oxygen-oxygen dumbbell (Figure 9a). The presence of $F_{2g}(\text{Li}^1\text{O}_4)$ in the deconvoluted Raman signal strongly suggests that the lithium diffusion follows the TSH mechanism, where some of the migrating lithium ions remain trapped in these tetrahedral lattice sites to accommodate the changes in coordination. The inherent asymmetries imposed by the Mn/Ti ions to the octahedral sites reduce the site energy of this transient tetrahedral site, favoring the o-t-o translation pathway.^{15,49,50,54}

The Raman spectra from successive charging of 1/3FL and 1/2FL materials are shown in Figure 8b,c. In both cases, the general Raman features remain the same, and both show a similar low-strain structural change (appearance of a spinel-type lattice) upon delithiation. The $F_{2g}(\text{Mn}^{\text{II}}\text{O}_6)$ and $E_g(\text{Mn}^{\text{II}}\text{O}_6)$ bands show little-to-no blue shift upon charging (Figure S10), proving the fact that the $\text{Mn}^{\text{II}}\text{O}_6$ moieties are structurally robust compared with those of 0FL. The main striking difference is observed in the $A_{1g}(\text{Mn}^{\text{III}}\text{O}_6)$ stretching vibration (Figure 8b), which starts to appear prominently from

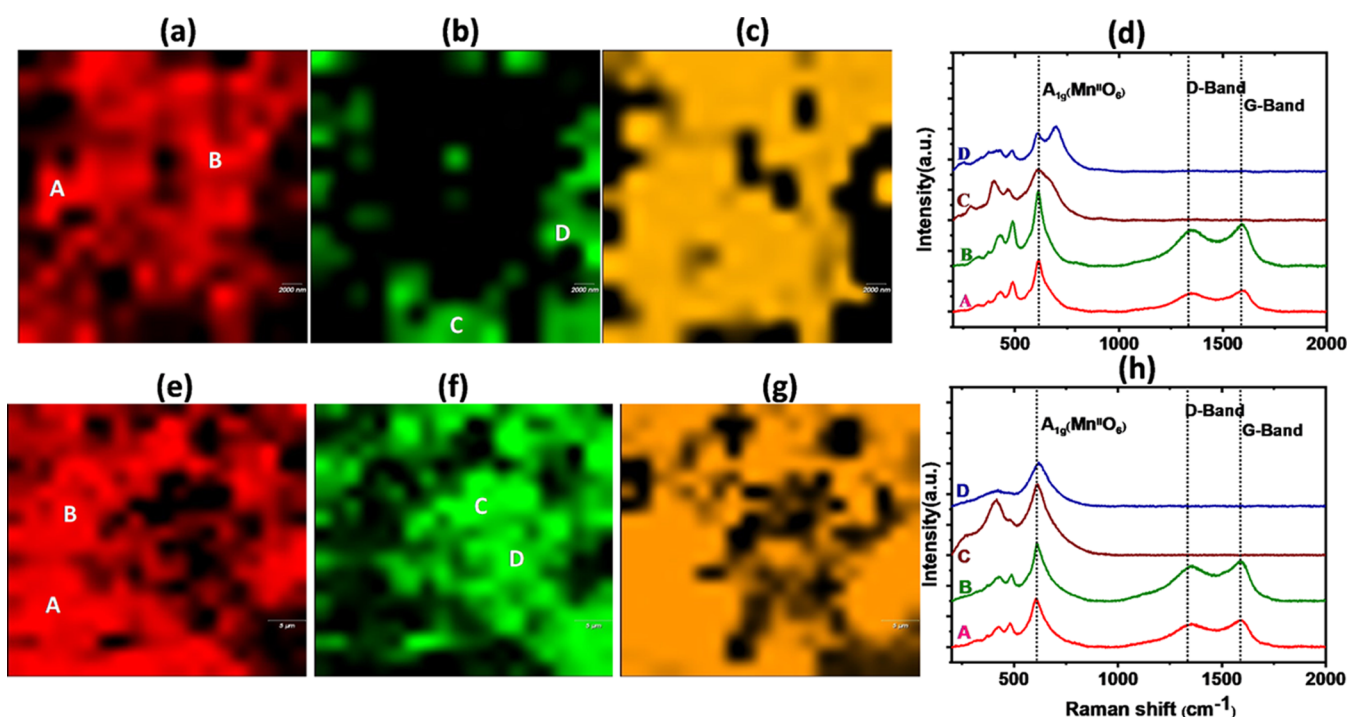


Figure 10. (a–c) Raman mapping of the 1/2FL cathode surface after 50 cycles; red: $Fm\bar{3}m$ -type structure, green: $Fm\bar{3}m$ structure excluded, orange: carbon additive. (d) Raman spectra at different locations in the maps. (e–h) The same Raman data after 100 cycles.

3.1 V charging and is broader in the case of 1/3FL than in OFL. This proves the point that the charge balance in the cathode is maintained by the oxidation of Mn^{II} to Mn^{III} . Interestingly, the $A_{1g}(Mn^{II}O_6)$ band does not appear in the case of charging the 1/2FL cathode (Figure 8c). In such a case of F-rich composition, the oxidation of Mn^{II} occurs on specific octahedral sites, where Mn^{III} is coordinated by fluorine. It can be presumed that fluoride replaces some of the oxides of $Mn^{II}O_6$ and forms $Mn^{II}O_{6-y}F_y$ octahedra, preferred mixed octahedral sites over $Mn^{II}O_6$ sites. This selective oxidation, in the close presence of a more electronegative F, increases the oxidation potential relative to the cases of OFL and 1/3FL systems, where the redox reaction happens mostly in the $Mn^{II}O_6$ octahedral core.¹⁵

Lithiated Cathodes. Figure 8d shows the Raman spectra of the discharged OFL cathode at different discharged potentials. During the discharge, the prominent Raman fingerprints remain similar to that of the charged case, indicating a similar structural change in the lithiation process. The appearance of the $F_{2g}(Li^I O_4)$ band near 360 cm^{-1} by discharging to 2.4 V and until 1.5 V confirms that the highly symmetric rock salt structure undergoes changes upon lithiation. The spectral shift for the bands $F_{2g}(Mn^{II}O_6)$ and $E_g(Mn^{II}O_6)$ remains unchanged (Figure S10). In the case of fluorinated cathodes, two new bands at 673 and 235 cm^{-1} start to appear as the degree of lithiation is increased. The fluorinated cathodes show the $F_{2g}(Ti^{IV}O_6)$ band near 235 cm^{-1} upon lithiation (Figure 8e,f). This low-frequency band is very weak and appears from the discharged state of 2.1–1.5 V. It is attributed to the F_{2g} bending vibration of $Ti^{IV}O_6$ and can be observed only in the presence of significant local ordering of $Ti^{IV}O_6$. The signature from this bending mode is absent in the discharged OFL cathodes. Previously, Raman spectral analysis of the pristine cathodes elucidated that Ti^{IV}/Li^I are coordinated by both oxides and fluorides. Furthermore, the evolution of

$A_{1g}(Ti^{IV}O_6)$ upon fluorination during lithiation agrees with a privileged $Ti-F$ coordination, which can be confirmed from the increase of the local ordering in $Ti^{IV}O_6$ octahedra after sufficient lithiation. This ordering can be attributed to the preferential lithiation to the void sites near the fluoride-rich part of the Ti^{IV}/Li^I lattice. This favorable lithium insertion may quench the fluoride ions from $Ti^{IV}O_{6-y}F_y$ toward the newly inserted lithium ions and make the $Ti^{IV}-O_6$ sites free. This kind of site-selective insertion of lithium and orientation of fluoride ions may strengthen the local ordering on the $Ti^{IV}O_6$ moiety, which may explain the appearance of the bending $F_{2g}(Ti^{IV}O_6)$ vibrational mode in the discharge.

Cyclability of the Cathodes. Complete structural preservation in successive charge–discharge cycles is crucial for better capacity retention and cyclability. Figure 9b represents the average intensity of the $F_{2g}(Li^I O_4)$ band with respect to the intensity of $A_{1g}(Mn^{II}O_6)$ during charging–discharging during the first cycle. The reduction of the relative intensity of this band on increasing the fluoride in the lattice suggests that less-mobile Li ions are trapped in the tetrahedral sites; hence, the possibility of ending up with a spinel-type modification is reduced. The increment of fluoride increases the efficiency of the lithium transport in between the octahedral sites by decreasing the structural inhomogeneity during charge–discharge processes. It can be assumed that the amount of active lithium, which can be leached and again inserted into the crystal lattice, is enhanced with the addition of fluorine in the lattice. This behavior is reflected in the better overall capacity in the case of 1/2FL composition.

The role of chemometrics in the analysis of Raman spectroscopic data is becoming increasingly important as it enables much detailed information to potentially qualify and quantify the different chemical/structural properties. We have performed multivariate method analysis to track cumulative changes in Raman spectra of the cathodes after several charge–

discharge cycles for direct visualization of the correlated structural information. Raman surface mapping of the 1/2FL cathode was carried out after 50 and 100 cycles, and a direct classical least square (DCLS in WiRE 4.0 software) component analysis was performed. Here, the Raman spectrum of the $Fm\bar{3}m$ phase (pristine cathode) is used as a reference for component mixture analysis. The analyzed Raman maps of different cycling states are presented in Figure 10 and compared to the pristine material (Figure S11). In Figure 10a,e, the parts with red areas correspond to the $Fm\bar{3}m$ structure, whereas the green areas (Figure 10b,f) show a more asymmetric structure compared with $Fm\bar{3}m$. Figure 10c,g shows the areas of the cathode where the Raman intensity of the carbon additive is higher. Figure 10d,h shows the corresponding individual Raman spectra from different regions mentioned in the maps. The component analysis through the DCLS method shows that on increasing the cycle number, the crystal structure of the cathode shows overall symmetry deviations from the simple DRS structure. It is difficult to figure out the individual components from the Raman map and hence the exact deformed crystal lattice. However, careful observation reveals the resemblance between the Raman maps created by the $Fm\bar{3}m$ phase (Figure 10a,e) component and the map containing the information of carbon additive (Figure 10c,g). This stark closeness demonstrates that the $Fm\bar{3}m$ lattice is likely to break down in the regions showing the absence of conductive carbon additive, where the poor electronic contact is expected to result in surface charge accumulation. Cycling proceeds more smoothly in carbon-rich regions with effective structural retention. This inherent inhomogeneity imposed by the electrically conducting and insulating or inactive phase hinders the continuous lithiation–delithiation and hence the partial fading of the effective capacity of the cathode. This direct evidence of phase transformation on the surface of the electrode corroborates the electrochemical cycling behavior and Mn-dissolution issues.

CONCLUSIONS

In this work, by varying the F/Li ratio, we investigated the $\text{Li}_{1+x}\text{Mn}_{2/3}\text{Ti}_{1/3}\text{O}_2\text{F}_x$ (LMTOF, $0 \leq x \leq 1$) DRS oxyfluorides as cathode materials for Li-ion batteries. The XRD and STEM data proved that after incorporating different amounts of fluorine, the disordered rock salt structure was successfully synthesized and maintained. The electrochemical analysis indicated that fluorination at high F/Li ratios can enhance the rate capability and the accessible reversible capacity during cycling. In this Li-rich DRS configuration, the charge-transfer resistance is decreased, contributing to the improvement of the Li^+ diffusion coefficient. In addition, fluorine alleviates the oxygen redox-active sites associated with Mn dissolution. Raman spectroscopy analysis conveys that with an increased amount of fluorine, the local ordering in LMTOF materials increases by reinforcing the ordering in the $\text{Mn}^{\text{II}}\text{O}_6$ octahedral active sites. Furthermore, the ex situ Raman spectra confirmed the stability of the $Fm\bar{3}m$ structure and shed light on the varying oxidation states of Mn ions during (de)lithiation by affirming the preferential coordination of F with Li and Ti. Upon delithiation, the bond angle $\text{O}-\text{Mn}^{\text{II}}-\text{O}$ decreases sequentially, and the Li^+O_4 tetrahedral appears to compensate for the changes in coordination and charge balance. However, with high F/Li ratios, the structure is preserved, thanks to the accommodated $\text{O}-\text{Mn}-\text{O}$ geometry, and a strong Mn–F coordination is suggested. It is assumed that F-enrichment

leads to better o–t–o percolation, where the amount of LiO_4 tetrahedral is lower, hence preventing the transition to a spinel-type structure. During lithiation of F-rich materials, TiO_6 increases on account of Li–F formation, which leads to significant local ordering and structural stability. Upon prolonged cycling, the DRS structure remains intact in the vicinity of the carbon additive; however, beyond this conducting region, a structural alteration persists attributed to the appearance of an asymmetric structure compared to $Fm\bar{3}m$. The elucidation of the charge–discharge mechanism and structure accommodation as a function of fluorination could result in the design of DRS cathode materials with better lithium transport efficiency and electrochemical cycling performance.

ASSOCIATED CONTENT

Supporting Information

The Supporting Information is available free of charge at <https://pubs.acs.org/doi/10.1021/acs.chemmater.1c04059>.

Comparison of the peak shift of the X-ray diffraction patterns; SEM-EDX mapping and elemental analysis; EELS spectra for Mn L-, Ti L-, and O K-edges and EELS elemental mapping; electrochemical properties of the OFL sample; differential capacity (dQ/dV) and CV plots; Nyquist plots of the impedance; ex situ XRD for OFL and 1/3FL samples; Raman spectra of Mn_2O_3 , Ti_2O_3 , and Li_2O as references; detailed Raman analysis of peak frequency (λ^{peak}) and band width of the spectral bands; spectral shift of $F_{2g}(\text{Mn}^{\text{II}}\text{O}_6)$ and $E_g(\text{Mn}^{\text{II}}\text{O}_6)$ with respect to the pristine material; Raman map of the pristine 1/2FL sample; and detailed structural parameters and elemental quantification analysis (EDX, ICP-OES) (PDF)

AUTHOR INFORMATION

Corresponding Authors

Abdel El Kharbachi – Helmholtz Institute Ulm (HIU), 89081 Ulm, Germany; orcid.org/0000-0003-4332-1544; Email: kharbachi@kit.edu

Maximilian Fichtner – Helmholtz Institute Ulm (HIU), 89081 Ulm, Germany; Institute of Nanotechnology, Karlsruhe Institute of Technology (KIT), 76021 Karlsruhe, Germany; Email: m.fichtner@kit.edu

Authors

Yasaman Shirazi Moghadam – Helmholtz Institute Ulm (HIU), 89081 Ulm, Germany

Sirshendu Dinda – Helmholtz Institute Ulm (HIU), 89081 Ulm, Germany

Georgian Melinte – Helmholtz Institute Ulm (HIU), 89081 Ulm, Germany; Institute of Nanotechnology, Karlsruhe Institute of Technology (KIT), 76021 Karlsruhe, Germany

Christian Kübel – Helmholtz Institute Ulm (HIU), 89081 Ulm, Germany; Institute of Nanotechnology, Karlsruhe Institute of Technology (KIT), 76021 Karlsruhe, Germany; orcid.org/0000-0001-5701-4006

Complete contact information is available at: <https://pubs.acs.org/10.1021/acs.chemmater.1c04059>

Author Contributions

The manuscript was written through contributions of all authors. All authors have given approval to the final version of the manuscript.

Notes

The authors declare no competing financial interest.

ACKNOWLEDGMENTS

This work contributes to the research performed at CELEST (Center for Electrochemical Energy Storage Ulm-Karlsruhe). The TEM characterization experiments were performed at the Karlsruhe Nano Micro Facility (KNMF), a Helmholtz research infrastructure operated at KIT.

REFERENCES

- (1) Whittingham, M. S. Lithium batteries and cathode materials. *Chem. Rev.* **2004**, *104*, 4271–4302.
- (2) Lee, J.; Urban, A.; Li, X.; Su, D.; Hautier, G.; Ceder, G. Unlocking the potential of cation-disordered oxides for rechargeable lithium batteries. *Science* **2014**, *343*, 519–522.
- (3) Lee, M.-J.; Lee, S.; Oh, P.; Kim, Y.; Cho, J. High Performance LiMn₂O₄ Cathode Materials Grown with Epitaxial Layered Nanostructure for Li-Ion Batteries. *Nano Lett.* **2014**, *14*, 993–999.
- (4) Liu, Q.; He, H.; Li, Z.-F.; Liu, Y.; Ren, Y.; Lu, W.; Lu, J.; Stach, E. A.; Xie, J. Rate-Dependent, Li-Ion Insertion/Deinsertion Behavior of LiFePO₄ Cathodes in Commercial 18650 LiFePO₄ Cells. *ACS Appl. Mater. Interfaces* **2014**, *6*, 3282–3289.
- (5) Striebel, K.; Shim, J.; Sierra, A.; Yang, H.; Song, X.; Kostecki, R.; McCarthy, K. The development of low cost LiFePO₄-based high power lithium-ion batteries. *J. Power Sources* **2005**, *146*, 33–38.
- (6) Goodenough, J. B.; Park, K.-S. The Li-ion rechargeable battery: a perspective. *J. Am. Chem. Soc.* **2013**, *135*, 1167–1176.
- (7) Yabuuchi, N.; Takeuchi, M.; Nakayama, M.; Shiiba, H.; Ogawa, M.; Nakayama, K.; Ohta, T.; Endo, D.; Ozaki, T.; Inamasu, T.; et al. High-capacity electrode materials for rechargeable lithium batteries: Li₃NbO₄-based system with cation-disordered rocksalt structure. *Proc. Natl. Acad. Sci. U.S.A.* **2015**, *112*, 7650–7655.
- (8) Rozier, P.; Tarascon, J. M. Li-rich layered oxide cathodes for next-generation Li-ion batteries: chances and challenges. *J. Electrochem. Soc.* **2015**, *162*, A2490.
- (9) Nakajima, K.; Souza, F. L.; Freitas, A. L. M.; Thron, A.; Castro, R. H. R. Improving Thermodynamic Stability of nano-LiMn₂O₄ for Li-Ion Battery Cathode. *Chem. Mater.* **2021**, *33*, 3915–3925.
- (10) Johnson, C.; Kim, J.; Lefief, C.; Li, N.; Vaughey, J.; Thackeray, M. The significance of the Li₂MnO₃ component in ‘composite’-x-Li₂MnO₃-(1-x) LiMnO₂. 5NiO. 5O₂ electrodes. *Electrochem. Commun.* **2004**, *6*, 1085–1091.
- (11) Bréger, J.; Jiang, M.; Dupré, N.; Meng, Y. S.; Shao-Horn, Y.; Ceder, G.; Grey, C. P. High-resolution X-ray diffraction, DIFFaX, NMR and first principles study of disorder in the Li₂MnO₃-Li [Ni_{1/2}Mn_{1/2}] O₂ solid solution. *J. Solid State Chem.* **2005**, *178*, 2575–2585.
- (12) House, R. A.; Jin, L.; Maitra, U.; Tsuruta, K.; Somerville, J. W.; Förstermann, D. P.; Massel, F.; Duda, L.; Roberts, M. R.; Bruce, P. G. Lithium manganese oxyfluoride as a new cathode material exhibiting oxygen redox. *Energy Environ. Sci.* **2018**, *11*, 926–932.
- (13) Thackeray, M. M.; Johnson, C. S.; Vaughey, J. T.; Li, N.; Hackney, S. A. Advances in manganese-oxide ‘composite’ electrodes for lithium-ion batteries. *J. Mater. Chem.* **2005**, *15*, 2257–2267.
- (14) Vu, N. H.; Arunkumar, P.; Won, S.; Kim, H. J.; Unithrattil, S.; Oh, Y.; Lee, J.-W.; Im, W. B. Effects of excess Li on the structure and electrochemical performance of Li_{1+x}MnTiO_{4+δ} cathode for Li-ion batteries. *Electrochim. Acta* **2017**, *225*, 458–466.
- (15) Euchner, H.; Chang, J. H.; Groß, A. On stability and kinetics of Li-rich transition metal oxides and oxyfluorides. *J. Mater. Chem. A* **2020**, *8*, 7956–7967.
- (16) Lee, J.; Kitchaev, D. A.; Kwon, D.-H.; Lee, C.-W.; Papp, J. K.; Liu, Y.-S.; Lun, Z.; Clement, R. J.; Shi, T.; McCloskey, B. D.; et al. Reversible Mn²⁺/Mn⁴⁺ double redox in lithium-excess cathode materials. *Nature* **2018**, *556*, 185–190.
- (17) Shirazi Moghadam, Y.; El Kharbachi, A.; Diemant, T.; Melinte, G.; Hu, Y.; Fichtner, M. Toward Better Stability and Reversibility of the Mn⁴⁺/Mn²⁺ Double Redox Activity in Disordered Rocksalt Oxyfluoride Cathode Materials. *Chem. Mater.* **2021**, *33*, 8235–8247.
- (18) Chen, R.; Ren, S.; Knapp, M.; Wang, D.; Witter, R.; Fichtner, M.; Hahn, H. Disordered Lithium-Rich Oxyfluoride as a Stable Host for Enhanced Li⁺ Intercalation Storage. *Adv. Energy Mater.* **2015**, *5*, No. 1401814.
- (19) Luo, Q.; Manthiram, A. Effect of Low-Temperature Fluorine Doping on the Properties of Spinel LiMn_{2-2y}Li_yM_yO_{4-η}F_η (M = Fe, Co, and Zn) Cathodes. *J. Electrochem. Soc.* **2009**, *156*, A84.
- (20) Dong, X.; Xu, Y.; Yan, S.; Mao, S.; Xiong, L.; Sun, X. Towards low-cost, high energy density Li₂MnO₃ cathode materials. *J. Mater. Chem. A* **2015**, *3*, 670–679.
- (21) Gao, C.; Zhou, J.; Liu, G.; Wang, L. Synthesis of F-doped LiFePO₄/C cathode materials for high performance lithium-ion batteries using co-precipitation method with hydrofluoric acid source. *J. Alloys Compd.* **2017**, *727*, 501–513.
- (22) Ren, S.; Chen, R.; Maawad, E.; Dolotko, O.; Guda, A. A.; Shapovalov, V.; Wang, D.; Hahn, H.; Fichtner, M. Improved Voltage and Cycling for Li⁺ Intercalation in High-Capacity Disordered Oxyfluoride Cathodes. *Adv. Sci.* **2015**, *2*, No. 1500128.
- (23) Takeda, N.; Hoshino, S.; Xie, L.; Chen, S.; Ikeuchi, I.; Natsui, R.; Nakura, K.; Yabuuchi, N. Reversible Li storage for nanosize cation/anion-disordered rocksalt-type oxyfluorides: LiMoO_{2-x}LiF (0 ≤ x ≤ 2) binary system. *J. Power Sources* **2017**, *367*, 122–129.
- (24) Richards, W. D.; Dacek, S. T.; Kitchaev, D. A.; Ceder, G. Fluorination of lithium-excess transition metal oxide cathode materials. *Adv. Energy Mater.* **2018**, *8*, No. 1701533.
- (25) Lun, Z.; Ouyang, B.; Kitchaev, D. A.; Clément, R. J.; Papp, J. K.; Balasubramanian, M.; Tian, Y.; Lei, T.; Shi, T.; McCloskey, B. D.; et al. Improved Cycling Performance of Li-Excess Cation-Disordered Cathode Materials upon Fluorine Substitution. *Adv. Energy Mater.* **2019**, *9*, No. 1802959.
- (26) Baur, C.; Kallquist, I.; Chable, J.; Chang, J. H.; Johnsen, R. E.; Ruiz-Zepeda, F.; Ateba Mba, J. M.; Naylor, A. J.; Garcia-Lastra, J. M.; Vegge, T.; et al. Improved cycling stability in high-capacity Li-rich vanadium containing disordered rock salt oxyfluoride cathodes. *J. Mater. Chem. A* **2019**, *7*, 21244–21253.
- (27) Baur, C.; Lăcătușu, M.-E.; Fichtner, M.; Johnsen, R. E. Insights into Structural Transformations in the Local Structure of Li₂VO₂F Using Operando X-ray Diffraction and Total Scattering: Amorphization and Recrystallization. *ACS Appl. Mater. Interfaces* **2020**, *12*, 27010–27016.
- (28) Yabuuchi, N.; Sugano, M.; Yamakawa, Y.; Nakai, I.; Sakamoto, K.; Muramatsu, H.; Komaba, S. Effect of heat-treatment process on FeF₃ nanocomposite electrodes for rechargeable Li batteries. *J. Mater. Chem.* **2011**, *21*, 10035–10041.
- (29) Lun, Z. Y.; Ouyang, B.; Cai, Z. J.; Clement, R.; Kwon, D. H.; Huang, J. P.; Papp, J. K.; Balasubramanian, M.; Tian, Y. S.; McCloskey, B. D.; et al. Design Principles for High-Capacity Mn-Based Cation-Disordered Rocksalt Cathodes. *Chem* **2020**, *6*, 153–168.
- (30) Nakajima, M.; Yabuuchi, N. Lithium-excess cation-disordered rocksalt-type oxide with nanoscale phase segregation: Li_{1.25}NbO_{3.5}VO₂. 5O₂. *Chem. Mater.* **2017**, *29*, 6927–6935.
- (31) Chang, J. H.; Baur, C.; Mba, J.-M. A.; Arçon, D.; Mali, G.; Alwast, D.; Behm, R. J.; Fichtner, M.; Vegge, T.; Lastra, J. M. G. Superoxide formation in Li₂VO₂F cathode material—a combined computational and experimental investigation of anionic redox activity. *J. Mater. Chem. A* **2020**, *8*, 16551–16559.
- (32) Im, J. C.; Vu, N. H.; Huu, H. T.; Lee, D. S.; Im, W. B. Effects of fluorine doping on electrochemical performance of spinel-layered Li₃Mn₃O₇. 5-xFx as cathode materials for Li-ion batteries. *J. Electrochem. Soc.* **2019**, *166*, A1568.

- (33) Takeda, N.; Ikeuchi, I.; Natsui, R.; Nakura, K.; Yabuuchi, N. Improved electrode performance of lithium-excess molybdenum oxyfluoride: titanium substitution with concentrated electrolyte. *ACS Appl. Energy Mater.* **2019**, *2*, 1629–1633.
- (34) Baur, C.; Chable, J.; Klein, F.; Chakravadhanula, V. S. K.; Fichtner, M. Reversible delithiation of disordered rock salt LiVO₂. *ChemElectroChem* **2018**, *5*, 1484–1490.
- (35) Ren, Q.; Yuan, Y.; Wang, S. Interfacial Strategies for Suppression of Mn Dissolution in Rechargeable Battery Cathode Materials. *ACS Appl. Mater. Interfaces* **2021**, DOI: 10.1021/acsami.1c20406.
- (36) Vortmann-Westhoven, B.; Lürenbaum, C.; Winter, M.; Nowak, S. Determination of lithium and transition metals in Li₁Ni_{1/3}Co_{1/3}Mn_{1/3}O₂ (NCM) cathode material for lithium-ion batteries by capillary electrophoresis. *Electrophoresis* **2017**, *38*, 540–546.
- (37) Park, T.-J.; Lim, J.-B.; Son, J.-T. Effect of calcination temperature of size controlled microstructure of LiNi_{0.8}Co_{0.15}Al_{0.05}O₂ cathode for rechargeable lithium battery. *Bull. Korean Chem. Soc.* **2014**, *35*, 357.
- (38) Jossen, A. Fundamentals of battery dynamics. *J. Power Sources* **2006**, *154*, 530–538.
- (39) Cambaz, M. A.; Vinayan, B. P.; Gesswein, H.; Schiele, A.; Sarapulova, A.; Diemant, T.; Mazilkin, A.; Brezesinski, T.; Behm, R. J.; Ehrenberg, H.; et al. Oxygen Activity in Li-Rich Disordered Rock-Salt Oxide and the Influence of LiNbO₃ Surface Modification on the Electrochemical Performance. *Chem. Mater.* **2019**, *31*, 4330–4340.
- (40) Chen, R.; Ren, S.; Yavuz, M.; Guda, A. A.; Shapovalov, V.; Witter, R.; Fichtner, M.; Hahn, H. Li⁺ intercalation in isostructural Li₂VO₃ and Li₂VO₂F with O²⁻ and mixed O²⁻/F⁻ anions. *Phys. Chem. Chem. Phys.* **2015**, *17*, 17288–17295.
- (41) Iliev, M.; Abrashev, M.; Litvinchuk, A.; Hadjiev, V.; Guo, H.; Gupta, A. Raman spectroscopy of ordered double perovskite La₂CoMnO₆ thin films. *Phys. Rev. B* **2007**, *75*, No. 104118.
- (42) Rousseau, D. L.; Bauman, R. P.; Porto, S. Normal mode determination in crystals. *J. Raman Spectrosc.* **1981**, *10*, 253–290.
- (43) Torres, D.; Freire, J.; Katiyar, R. Lattice dynamics of crystals having R₂MX₆ structure. *Phys. Rev. B* **1997**, *56*, 7763.
- (44) Julien, C.; Massot, M. Raman spectroscopic studies of lithium manganates with spinel structure. *J. Phys.: Condens. Matter* **2003**, *15*, 3151.
- (45) Amalraj, F.; Kovacheva, D.; Talianker, M.; Zeiri, L.; Grinblat, J.; Leifer, N.; Goobes, G.; Markovsky, B.; Aurbach, D. Synthesis of Integrated Cathode Materials xLi₂MnO₃ - (1-x)LiMn_{1/3}Ni_{1/3}Co_{1/3}O₂ (x = 0.3, 0.5, 0.7) and Studies of Their Electrochemical Behavior. *J. Electrochem. Soc.* **2010**, *157*, A1121–A1130.
- (46) Julien, C. M.; Mauger, A. In situ Raman analyses of electrode materials for Li-ion batteries. *AIMS Mater. Sci.* **2018**, *5*, 650–698.
- (47) Mukai, K.; Kato, Y.; Nakano, H. Understanding the zero-strain lithium insertion scheme of Li [Li_{1/3}Ti_{5/3}]O₄: structural changes at atomic scale clarified by Raman spectroscopy. *J. Phys. Chem. C* **2014**, *118*, 2992–2999.
- (48) Pelegov, D. V.; Slautin, B. N.; Gorshkov, V. S.; Zelenovskiy, P. S.; Kiselev, E. A.; Kholkin, A. L.; Shur, V. Y. Raman spectroscopy, “big data”, and local heterogeneity of solid state synthesized lithium titanate. *J. Power Sources* **2017**, *346*, 143–150.
- (49) Clément, R. J.; Lun, Z.; Ceder, G. Cation-disordered rocksalt transition metal oxides and oxyfluorides for high energy lithium-ion cathodes. *Energy Environ. Sci.* **2020**, *13*, 345–373.
- (50) Chen, D.; Ahn, J.; Self, E.; Nanda, J.; Chen, G. Understanding cation-disordered rocksalt oxyfluoride cathodes. *J. Mater. Chem. A* **2021**, *9*, 7826–7837.
- (51) Julien, C.; Massot, M.; Baddour-Hadjean, R.; Franger, S.; Bach, S.; Pereira-Ramos, J. P. Raman spectra of birnessite manganese dioxides. *Solid State Ionics* **2003**, *159*, 345–356.
- (52) Hua, W.; Wang, S.; Knapp, M.; Leake, S. J.; Senyshyn, A.; Richter, C.; Yavuz, M.; Binder, J. R.; Grey, C. P.; Ehrenberg, H.; et al. Structural insights into the formation and voltage degradation of lithium- and manganese-rich layered oxides. *Nat. Commun.* **2019**, *10*, No. 5365.
- (53) Van der Ven, A.; Ceder, G. Lithium diffusion mechanisms in layered intercalation compounds. *J. Power Sources* **2001**, 97–98, 529–531.
- (54) Ji, H.; Urban, A.; Kitchaev, D. A.; Kwon, D.-H.; Artrith, N.; Ophus, C.; Huang, W.; Cai, Z.; Shi, T.; Kim, J. C.; et al. Hidden structural and chemical order controls lithium transport in cation-disordered oxides for rechargeable batteries. *Nat. Commun.* **2019**, *10*, No. 592.

Recommended by ACS

Reductive Decomposition Kinetics and Thermodynamics That Govern the Design of Fluorinated Alkoxyaluminate/Borate Salts for Mg-Ion and Ca-Ion Batt...

Xiaowei Xie, Kristin A. Persson, et al.

NOVEMBER 30, 2022
THE JOURNAL OF PHYSICAL CHEMISTRY C

READ 

Controlling the Cathodic Potential of KVPO₄F through Oxygen Substitution

Romain Wernert, Laurence Croguennec, et al.

MAY 03, 2022
CHEMISTRY OF MATERIALS

READ 

Exploring the Origin of Anionic Redox Activity in Super Li-Rich Iron Oxide-Based High-Energy-Density Cathode Materials

Zhenpeng Yao, Chris Wolverton, et al.

MAY 04, 2022
CHEMISTRY OF MATERIALS

READ 

How Fluorine Introduction Solves the Spinel Transition, a Fundamental Problem of Mn-Based Positive Electrodes

Yuji Mahara, Yoshinari Makimura, et al.

MAY 17, 2022
ACS APPLIED MATERIALS & INTERFACES

READ 

Get More Suggestions >